

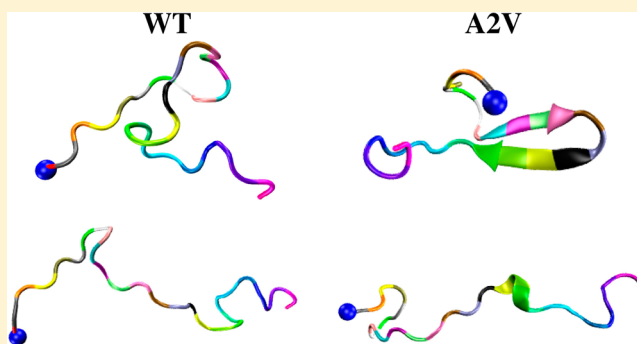
# Familial Alzheimer A2 V Mutation Reduces the Intrinsic Disorder and Completely Changes the Free Energy Landscape of the A $\beta$ 1–28 Monomer

Phuong H. Nguyen,<sup>†</sup> Bogdan Tarus,<sup>†</sup> and Philippe Derreumaux<sup>\*,†,‡</sup>

<sup>†</sup>Laboratoire de Biochimie Théorique, UPR 9080 CNRS, Université Paris Diderot, Sorbonne Paris Cité, IBPC, 13 rue Pierre et Marie Curie, 75005 Paris, France

<sup>‡</sup>Institut Universitaire de France, IUF, 103 Boulevard Saint-Michel, 75005 Paris, France

**ABSTRACT:** The self-assembly of the amyloid- $\beta$  (A $\beta$ ) peptide of 39–43 amino acids into senile plaques is one hallmark of Alzheimer's disease (AD) pathology. While A2 V carriers remain healthy in the heterozygous state, they suffer from early onset AD in the homozygous state. As a first toward understanding the impact of A2 V on A $\beta$  at its earlier stage, we characterized the equilibrium ensemble of the A $\beta$ 1–28 wild type and A $\beta$ 1–28 A2 V monomers by means of extensive atomistic replica exchange molecular dynamics simulations. While global conformational properties such as the radius of gyration and the average secondary structure content of the whole peptides are very similar, the population of  $\beta$ -hairpins is increased by a factor of 4 in A2 V, and this may explain the enhanced A $\beta$ 1–40 A2 V aggregation kinetics with respect to A $\beta$ 1–40 wild type. Both peptides display a non-negligible population of extended metastable conformations differing however in their atomic details that represent ideal seeds for polymerization. Remarkably, upon A2 V mutation, the intrinsic disorder of A $\beta$ 1–28 monomer is reduced by a factor of 2, and the free energy landscape is completely different. This difference in the conformational ensembles of the two peptides may explain in part why the mixture of the A $\beta$ 40 WT and A2 V peptides protects against AD.



## 1. INTRODUCTION

Alzheimer's disease (AD) is a progressive irreversible neurological disorder with marked atrophy of cerebral cortex and loss of cortical and subcortical neurons. AD is characterized by accumulation of amyloid plaques, and numerous neurofibrillary tangles formed from filaments of highly phosphorylated tau proteins. The major constituents of the plaques are made of amyloid- $\beta$  (A $\beta$ ) proteins of 39–43 amino acids.<sup>1</sup> A $\beta$  peptide is formed by proteolytic processing of the amyloid precursor protein (APP) catalyzed by the  $\beta$ - and  $\gamma$ -secretases. Despite the number of drugs tested, all of them have failed to slow the progression of AD in clinical trials.<sup>2</sup>

For simplicity, all A $\beta$ 1-xx peptides will be designated as A $\beta$ xx. The A $\beta$ 42 peptide contains a hydrophilic and charged N-terminus (A1-K16) and two hydrophobic patches L17-A21 and A30-A42 separated by a hydrophilic patch E22-G29. The physical factors underlying amyloid formation are difficult to describe because A $\beta$  generates a wide variety of structures in vitro, depending on the exact aggregation conditions, i.e., agitation, and sample preparation.<sup>3,4</sup> The oligomer size distribution, the lag phase and the final product also vary from A $\beta$ 40 to A $\beta$ 42, and upon the presence of familial (K16N, A21G, E22G, E22Q, E22K, E22 $\Delta$ , and D23N) and nonfamilial (K16A, F19P, G33A, and G33I) mutations.<sup>5,6</sup> Fibrils of synthetic A $\beta$ 42 peptides display U-shaped conformations with

$\beta$ -strands spanning the residues 17–20 and 31–40 with the 16 N-terminal residues disordered, while fibrils of synthetic A $\beta$ 40 peptides have  $\beta$ -strands at 10–23 and 30–38 with the 9 N-terminal residues disordered. There is also recent experimental evidence that fibrils made of AD-brain derived A $\beta$ 40 peptides show deformed U-shaped conformations, with in a twist in residues F19-D23, a kink at G33, and a bend at G37-G38, and the fibril structure varies from one patient to another.<sup>7</sup>

Because the first disease-causing mutations were observed at positions 21–23,<sup>8</sup> and the N-terminus is highly disordered in the final fibril state,<sup>4</sup> it is believed that the N-terminal residues do not play any critical role in aggregation. Several theoretical and experimental results, however, contradict this paradigm.

First, it has been shown that the double mutation D1E/A2 V affects A $\beta$ 40 fibrillogenesis.<sup>9</sup> Pulse EPR spectroscopy of A $\beta$ 16 peptide also evidenced the key role of D1 and A2 in the coordination of copper ion.<sup>10</sup> This is not surprising since disease-associated modifications involving the first three amino acids have been long known. These include isomerization at D1 and proteolytic removal of D1 and A2 and the subsequent cyclizing of E3 to a pyroglutamate.<sup>8</sup>

**Received:** November 24, 2013

**Revised:** December 21, 2013

**Published:** December 29, 2013

Second, other changes in the terminus, the H6R (English), D7H (Taiwanese), and D7N (Tottori) familial mutations, have been identified,<sup>11,12</sup> and the H6R and D7N mutations have been found to alter A $\beta$ 40/42 assembly at its earliest stages, including monomer folding and oligomers.<sup>13</sup>

Third, coarse-grained simulations of the dimers of A $\beta$ 40 and A $\beta$ 42 peptides using two distinct force fields<sup>14–17</sup> and dimers of A $\beta$ 28<sup>18</sup> reported the existence of transient  $\beta$ -sheets formed by the residues 3–13. Though both force fields average out many degrees of freedom and treat solvent effects implicitly, Urbanc et al. reproduced differences in oligomer size distributions between A $\beta$ 40 and A $\beta$ 42 consistent with experiments,<sup>15</sup> and OPEP-based simulations identified reptation moves between the strands<sup>19,20</sup> and observed  $\beta$ -barrels<sup>21–23</sup> during self-assembly of amyloid peptides that were validated by FTIR,<sup>21</sup> X-ray crystallography<sup>24</sup> and atomistic simulations.<sup>25</sup> OPEP simulations also proposed inhibition mechanisms of A $\beta$ 16–22 protofibril consistent with experiments,<sup>26</sup> and transient  $\beta$ -sheets displaying a variety of sheet-to-sheet pairing angles<sup>23,27</sup> that were also revealed by crystal structures of macrocyclic  $\beta$ -sheet mimics.<sup>28</sup>

Fourth, using a combination of NMR solvent protection experiments and computational structural screening, highly flexible A $\beta$ 42 pentamers display an amyloid structural motif of a triple  $\beta$ -sheet, with the N-terminal residues interacting with the core (K16-E22)  $\beta$ -sheet region.<sup>29</sup> Using solid state NMR spectroscopy, a toxic A $\beta$ 40 oligomer of high molecular weight was identified with a  $\beta$ -sheet at the N-terminus.<sup>30</sup> Using single-molecule atomic force spectroscopy, the N-terminal region was found to play an important role in dimeric A $\beta$ 40/42 interactions,<sup>31</sup> consistent with coarse-grained,<sup>14–16,32</sup> and all-atom simulations.<sup>33,34</sup>

Finally, two new familial and particularly intriguing mutations were reported in the N-terminus. A genetic mutation in an Italian family, A2 V, caused an early onset of AD when it is only inherited from both parents, while heterozygous carriers of A2 V were unaffected. In other terms, A2 V enhances A $\beta$ 40 aggregation kinetics, but the mixture of the A $\beta$ 40 WT and A2 V peptides protects against AD.<sup>35</sup> The second striking result comes from the analysis of APP in a set of whole-genome sequence data from 1795 Icelanders and the discovery that the mutation A2T protects against AD in both heterozygous and homozygous carriers.<sup>36</sup>

The goal of this study is to determine the differences in the structures and free energy surfaces of the monomer of A $\beta$  wild type (WT) and A $\beta$  A2 V by means of extensive atomistic replica exchange molecular dynamics (REMD) simulations. By using Langevin dynamics of a mesoscopic model, and Monte Carlo simulations of a lattice model, it has been demonstrated that the population of the amyloid-competent monomeric state, which results from the balance between electrostatic and hydrophobic interactions, impacts both the nucleus size and the lag phase as well as the topology of the fibrils.<sup>37,38</sup> Knowledge of the free energy surface of the monomer provides therefore valuable insights into the full aggregation process.

Here, we focus on the A $\beta$ 28 peptide rather than the A $\beta$ 40/42 peptides for the following reasons. A $\beta$ 28 forms amyloid fibrils characterized by in register parallel  $\beta$ -sheets as in the A $\beta$ 40 and A $\beta$ 42 fibrils.<sup>39</sup> The  $\gamma$ -secretase generates essentially peptides from A $\beta$ 36 to A $\beta$ 43,<sup>8</sup> but A $\beta$ 30 and A $\beta$ 26 peptides have also been reported by mass spectrometry analyses of human AD brains.<sup>40</sup> Thus by discarding the C-terminal, our study allows

determining the impact of the A2 V substitutions on the interactions between the NT (residues 1–16), CHC (central hydrophobic core, residues 17–21), and LR (loop, residues 22–28) regions, i.e., the three regions where all human disease-causing mutations are identified. A recent study based on electrospray ionization mass spectrometry also showed that that low molecular weight compounds bind similarly to A $\beta$ 42, A $\beta$ 40, and A $\beta$ 28 peptides.<sup>41</sup> Finally, this truncated peptide enables us to obtain reliable simulation statistics, and A $\beta$ 28 being much less prone aggregation than A $\beta$ 40 and A $\beta$ 42, our predictions can be tested experimentally.

While the effects of mutations at positions 21–23 on the monomer and dimer of A $\beta$ 40/42 and shorter fragments have been extensively studied by computational means,<sup>15,42–45</sup> the impact of the A2 V mutation on the monomer remains to be investigated experimentally and theoretically. We also determine how our REMD results on A $\beta$ 28 WT fit with available experimental data and previous explicit and implicit solvent all-atom simulations and coarse-grained simulations.

## 2. MATERIAL AND METHODS

**Simulation Details.** A $\beta$ 28 sequence is DAEFRHDSGY EVHHQKL VFF AEDVGSNK. The initial coordinates were taken from PDB (code: 1BA4). This A $\beta$ 40 conformation observed by NMR in an apolar environment is characterized by two  $\alpha$ -helices spanning residues 8–25 and 28–39.<sup>46</sup> We used the CHARMM22\* force field rather than the GROMOS and OPLS force field<sup>47</sup> because it allows folding diverse proteins into their NMR structures.<sup>48</sup> This force field has, however, some limitations for reproducing melting temperatures<sup>48</sup> and vibrational frequency modes with accuracy.<sup>49–51</sup>

A $\beta$  was initially put in the center of a truncated octahedron box with periodic boundary conditions and a volume of 9.4 nm<sup>3</sup> with 3000 TIP3P water molecules. To mimic buffers made of H<sub>2</sub>KPO<sub>4</sub> and adjusted with H<sub>2</sub>SO<sub>4</sub>, we added 5 mM [H<sub>2</sub>PO<sub>4</sub><sup>−</sup>], 5 mM [H<sub>1</sub>PO<sub>4</sub><sup>2−</sup>], and 20 mM [K<sup>+</sup>] (so SO<sub>4</sub> are neglected). The pH was set to 7 with the N-terminus NH<sub>3</sub><sup>+</sup> and C-terminus CO<sub>2</sub><sup>−</sup>, the Arg and Lys residues positively charged (NH<sub>3</sub><sup>+</sup>), the Glu and Asp residues negatively charged (CO<sub>2</sub><sup>−</sup>), and the His residues neutral with an hydrogen on the epsilon nitrogen site.

The GROMACS program (version: 4.5.5)<sup>52</sup> was used to perform the REMD simulations with an integration time step of 2 fs using the SHAKE method.<sup>53</sup> The particle mesh Ewald method with a cutoff of 1.1 nm was used for the electrostatic interactions, and a cutoff of 1.2 nm was used for the van der Waals interactions. The nonbonded pair lists were updated every 10 fs. Temperatures were controlled by the velocity-rescaling thermostat, developed by Bussi-Donadio-Parinello and found to sample the canonical ensemble.<sup>54</sup>

To obtain the initial WT structure for REMD, a 5 ns MD simulation at 500 K was performed starting from the  $\alpha$ -helical conformation, and the last random coil structure was selected. The structure for A2 V was obtained from the WT final structure by using the mutation tools in pymol.<sup>55</sup> For each system, REMD was carried out with 48 replicas varying from 290 to 466 K using the temperature method developed by Patriksson and van der Spoel.<sup>56</sup> Exchanges between neighboring replicas were attempted every 2 ps, leading to an average acceptance ratio of 25%. Each replica ran for 205 ns, and we excluded the first 50 ns for analysis.

**Analysis.** The secondary structures were calculated using STRIDE.<sup>57</sup> We grouped the eight structures defined by

STRIDE into four structures:  $\beta$ -strand = extended + bridge,  $\alpha$ -helix =  $\alpha$ -helix +  $3_{10}$ -helix + PII-helix, turn = turn + bend, and coil = coil. Note that the percentage of  $3_{10}$ -helix + PII-helix is marginal in the present simulations. A C $\alpha$ -C $\alpha$  contact was defined if the distance is less than 5 Å. A side-chain – side-chain (Sc) contact was considered formed if the distance between their centers of mass is <6.5 Å. A salt-bridge (SB) between two charged residues was considered formed if the distance between two specific atoms remains within 4.6 Å.<sup>45</sup> A hydrogen bond (H-bond) was considered formed when the acceptor–donor distance is not more than 3.5 Å, and the acceptor–donor–hydrogen angle is not more than 30°. We defined a topological descriptor ranging from a two-stranded  $\beta$ -sheet or  $\beta$ -hairpin to a three-stranded  $\beta$ -sheet with the requirement that in all cases there are at least two backbone H-bonds formed between consecutive  $\beta$ -strands, and there are in each strand at least three consecutive residues in the  $\beta$  Ramachandran region.<sup>45</sup>

We also analyzed the conformations using two metrics, the root-mean square deviation (RMSD) and the principal component analysis (PCA).<sup>58</sup> The C $\alpha$  RMSD clustering was done using the linkage algorithm with a cutoff of 0.25 or 0.15 nm. For disordered peptides, the RMSD and the PCA of the dihedral angles are not very informative, however, and we found that the inverse distances between C $\alpha$  atoms are more appropriate to describe the collective motions.<sup>45</sup> To facilitate a direct comparison between the two systems, it is important to use the same eigenvectors. To this end, we combined the two trajectories and performed PCA by projecting the trajectory of each system on the obtained eigenvectors. In our systems, the first three principal components, V1, V2, and V3, account for up to 60% of the fluctuations. To identify geometric clusters in this subspace, we carried out clustering analysis using the Hartigan–Wong  $k$ -means algorithm<sup>59</sup> as implemented in the R program suite.<sup>60</sup> As discussed in ref 61, this procedure yields the correct numbers of minima and barriers of the free energy landscape, while being much faster than performing clustering on the full space data set. As the  $k$ -means clustering is sensitive to the initial conditions, the algorithm was run 2000 times, and the best results were chosen. To determine the optimal value of the number of clusters ( $k = 15$  for WT and  $k = 12$  for A2 V), we examined the sum of squares of the observations to their assigned cluster centers and the 30 most popular indices for cluster validation provided by the NbClust package,<sup>62</sup> and we performed a visual inspection of the partitioning. Statistical errors were estimated by block (time interval) averaging.

### 3. RESULTS

**REMD Convergence.** We assessed convergence at 315 K, near physiological temperature, by using five metrics and either two or three time intervals (50–150 and 50–205 ns or 50–102, 102–154, and 154–205 ns). These metrics include the distribution of the radius of gyration ( $R_g$ ), the distribution of C $\alpha$  end-to-end distances, the distribution of the total number of C $\alpha$  contacts, and the solvent accessible surface area (SASA) of each amino acid. As seen in Figure 1, the three distributions for WT and A2 V remain constant as the time progresses from 150 to 205 ns. Similarly, the SASA profiles along the amino acid sequence do not change using the two time intervals. Figure 1 also shows the turn content of each WT and A2 V residue using three distinct time windows. We see that the statistical errors remain low. Small errors are also observed for the coil,  $\alpha$ -helix and  $\beta$ -strand contents along the sequences (data not shown).

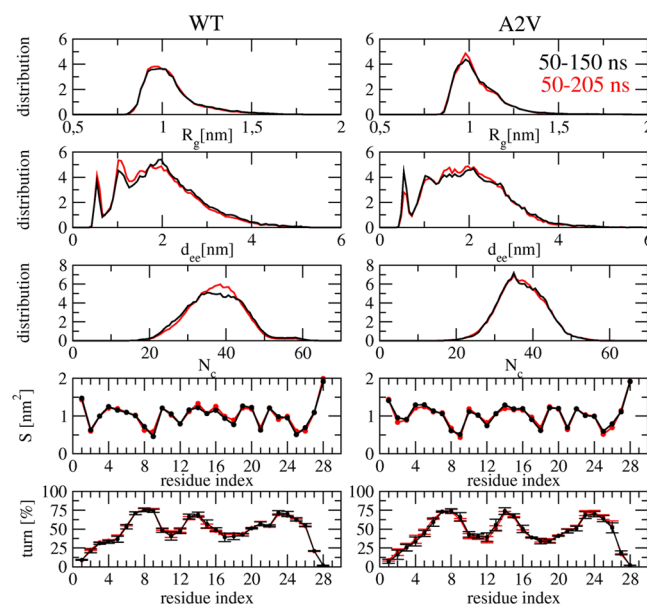


**Figure 1.** Convergence of REMD simulations at 315 K for the WT (left) and A2 V (right) peptides. Distributions of the radius of gyration ( $R_g$ ), C $\alpha$  end-to-end distance ( $d_{ce}$ ), total number of the C $\alpha$  contacts ( $N_c$ ), and the solvent accessible surface area of each amino acid ( $S$ ). Shown are results obtained using the time intervals of 50–150 (black) and 50–205 ns (red). The last panel shows the turn propensity of each amino acid with the statistical errors estimated by using the three time intervals of 50–102, 102–154, and 154–205 ns.

Taken together these results indicate that both simulations have converged within 205 ns.

Comparing the results between WT and A2 V, the radius of gyration and end-to-end distance distributions are almost identical, and the distributions of C $\alpha$  contacts and the SASA profiles superpose well, indicating similar average global conformational properties. It is found that 86, 45 and 11% of the A2 V conformations, and 85, 40 and 10% of the WT conformations, have C $\alpha$  end-to-end distances >1, >2, and >3 nm, respectively, indicating extended and unfolded conformations rather than compact states. The radius of gyration, which varies from 0.6 nm to mainly 1.25 nm, also supports this lack of compactness. We also observe that most residues are exposed to solvent ( $SASA > 1 \text{ nm}^2$ ), with the exceptions of the residues Glu3, Ser8, Val12, Val18, and Ser26 and, the residues with small side chains, Ala2 in WT and Val2 in the mutant, Gly9, Ala21, and Gly25.

**Secondary Structures and Salt-Bridges.** The mutation does not change the secondary structure of the whole peptide, but changes the secondary structure propensity of some amino acids at 315 K. The coil and turn dominate at  $34 \pm 1.8\%$  and  $48 \pm 1.5\%$  in WT vs  $35 \pm 2.0\%$  and  $46 \pm 2.6\%$  in A2 V. The  $\beta$ -strand and  $\alpha$ -helix contents remain at  $10 \pm 2.1\%$  and  $7 \pm 1.3\%$  in WT vs  $11 \pm 1.3\%$  and  $7 \pm 1.4\%$  in A2 V. Figure 2 shows the  $\beta$ -strand,  $\alpha$ -helix, turn, and coil contents along the sequence. The  $\alpha$ -helix, turn and coil profiles are overall very similar between WT and A2 V. Turns are observed at residues 6–9, 13–15 and 23–26 (probability >50%), and all residues, except the two N- and C-terminal residues, have a probability <50% to be random coil. Upon A2 V mutation, the turn character of residues 2, Glu3, Gly9, Val12, His13, Phe20, and Ala21 decreases by 5–13%, and the coil character of residues Gly9, Phe19, Phe20, and Ala21 increases by  $\sim 10\%$ . Three regions, around residues 2–5, 10–13, and 16–20 display pronounced



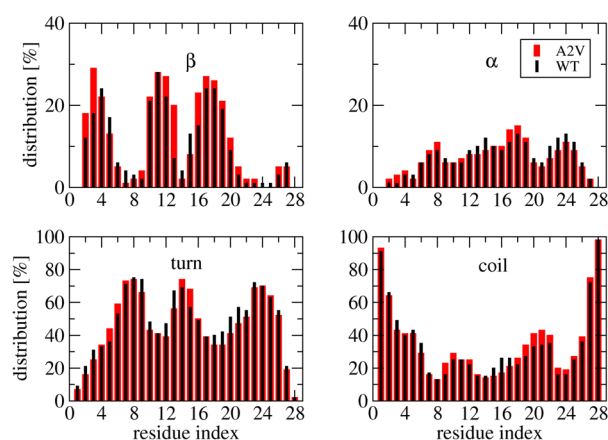


**Figure 2.** Secondary structure propensities of each amino acid at 315K: WT (black) and A2 V (red). Shown are results obtained using the time interval of 50–205 ns. For clarity, we zoom in the distributions of the  $\alpha$  and  $\beta$  panels.

$\beta$ -strand propensity (10–30% of the time) in both species. Upon A2 V mutation, however, the  $\beta$ -strand propensity of residues 2, Glu3, His13 and Lys16 increases from 11 to 17%, 17 to 28%, 6 to 19%, and 14 to 22%, while the  $\beta$ -strand propensity of residues Arg5 and Gln15 decreases from 16 to 13% and from 13 to 7%. Finally, all residues 2–27 have a low  $\alpha$ -helix propensity varying from 2 to 14% in both species.

Table 1 reports the lifetimes of all possible salt bridges (SB) between the charged residues at 315 K. It is found that the lifetime of the 18 SB's does not change significantly from WT to A2 V, with a maximum difference of 3.5% for the SB between Glu3 and Lys16. Overall, Arg5 has the highest probability ( $\sim 16 \pm 0.8\%$ ) to form a SB with both Glu3 and Glu7. Lys16 has the highest propensity to form a SB with Glu11 and Asp7 ( $7$  and  $6 \pm 0.8\%$ ), while Lys28 has the highest probability to form a SB with Asp23 ( $11.7 \pm 1.0\%$ ) and then Glu22 ( $6 \pm 0.7\%$ ). Note that the statistical errors in the lifetimes do not exceed 1.4%. Table 1 also reports the probability to observe a turn centered at residues 22–23, a structural characteristic of a toxic conformer of A $\beta$ 42.<sup>63</sup> It is found that WT has a higher turn probability ( $36 \pm 3\%$ ) than A2 V ( $26.7 \pm 2.8\%$ ).

**WT and A2 V Are Intrinsically Disordered but A2 V Has More Aggregation-Prone States.** Figure 3 shows the equilibrium populations of the configurations at 315 K using a 0.25 nm  $C\alpha$  RMSD cutoff and the full sequences. WT and A2T peptides have 2057 and 1322 clusters, respectively. None of the states dominate the free energy landscape, the most populated states having a probability of 2.3% and 3.7% in WT and A2 V, respectively, thereby confirming the intrinsically disordered

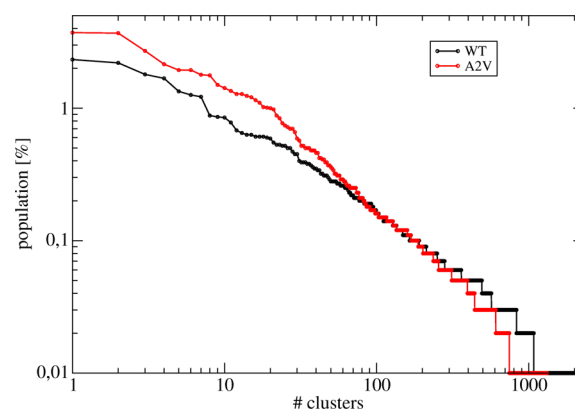


**Figure 3.** Equilibrium population of all clusters for the WT (black) and A2 V (red) peptides at 315 K. For clarity, log scales are used. Shown are results obtained using the time interval of 50–205 ns.

nature of the peptides. Combining the two trajectories and using the same RMSD cutoff, we find that 49.4% of the clusters are specific to WT, 49.1% are specific to A2 V, and only 4 or 1.5% of the clusters contain both WT and A2 V conformations, indicating the high structural dissimilarity between the two peptides. Note that the four common clusters are coil-turn. Performing the same analysis with a 0.15 nm  $C\alpha$  RMSD cutoff for various peptide lengths, we find that only 31% of the clusters contain both WT and A2 V states using residues 1–16, and the percentage drops to 10%, 2%, and 0.0001% using residues 1–20, 1–24, and 1–28, respectively.

To get insights into the equilibrium ensembles, Figures 4 and 5 show the dominant clusters of A $\beta$  WT and A $\beta$ A2 V on the subspace spanned by the first three principal components, V1, V2, and V3. We can identify 15 and 12 metastable minima for the WT and A2 V peptides, and a representative structure of each minimum is shown. Table 2 gives, for each cluster, its population, the average secondary structure composition, the average population of H-bonds between two  $\beta$ -strands, the average population of two-stranded  $\beta$ -sheets or  $\beta$ -hairpins (P2s), and the average  $C\alpha$  end-to-end distance. The average values are obtained by using all conformations belonging to each cluster. We also give the  $C\alpha$  RMSD of all minima with respect to the most populated minimum. Given the high flexibility of the peptides, a one-to-one comparison between the minima is not reasonable and we compare the common and different features between the peptides.

Looking at the structural features of the minima, we find that the first six minima of A2 V, representing 60% of all conformations, have a  $\beta$ -strand content varying from 4 to 24% and a probability of forming  $\beta$ -hairpins, P2s, varying between 7 and 24% (Table 2). In contrast, the first six

**Table 1. Probability (in %) of Forming Salt-Bridges between All Charged Residues and the Population of the Turn,  $P_{\text{turn}}$  (in %), Centered at Residues 22–23<sup>a</sup>**

system	res	Asp1	Glu3	Asp7	Glu11	Glu22	Asp23	$P_{\text{turn}}$
WT	Arg5	$2.68 \pm 0.77$	$15.77 \pm 0.26$	$15.97 \pm 0.61$	$3.22 \pm 0.60$	$1.48 \pm 0.39$	$5.22 \pm 0.54$	$36.10 \pm 2.94$
	Lys16	$2.66 \pm 0.63$	$2.26 \pm 0.29$	$6.04 \pm 0.75$	$7.15 \pm 0.49$	$1.80 \pm 0.18$	$2.87 \pm 0.31$	
	Lys28	$2.80 \pm 0.11$	$3.31 \pm 0.19$	$1.52 \pm 0.44$	$1.00 \pm 0.28$	$6.38 \pm 0.75$	$11.72 \pm 1.03$	
A2 V	Arg5	$2.77 \pm 0.43$	$16.31 \pm 0.81$	$14.23 \pm 0.51$	$5.61 \pm 0.67$	$3.06 \pm 0.31$	$2.87 \pm 0.63$	$26.73 \pm 2.78$
	Lys16	$2.86 \pm 1.24$	$5.93 \pm 0.30$	$3.90 \pm 0.81$	$6.82 \pm 1.41$	$1.12 \pm 0.22$	$2.19 \pm 0.53$	
	Lys28	$2.34 \pm 0.53$	$3.12 \pm 0.85$	$2.55 \pm 0.26$	$1.28 \pm 0.33$	$6.31 \pm 0.38$	$10.24 \pm 0.94$	

<sup>a</sup>The error bars were obtained from block averaging with three equal blocks from 50 to 205 ns at 315 K.

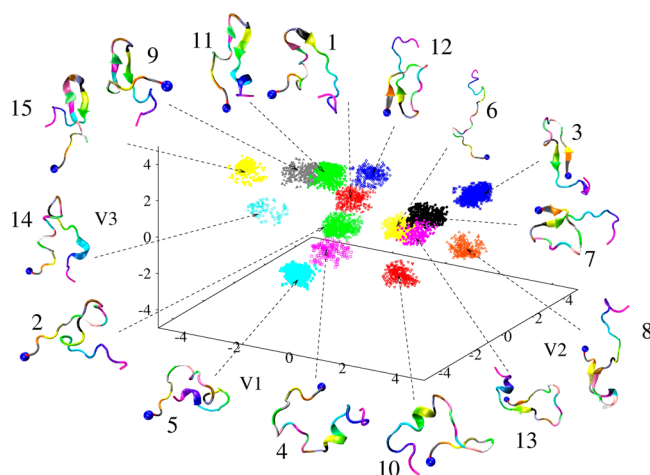


**Figure 4.** 15 clusters of the WT peptide on the subspace spanned by the first three principal components V1, V2, and V3. For clarity, only 200 data points around each cluster center are displayed. The representative structure of each cluster is also shown. The ball indicates the first residue. Shown are results obtained using the time interval of 50–205 ns at 315 K.

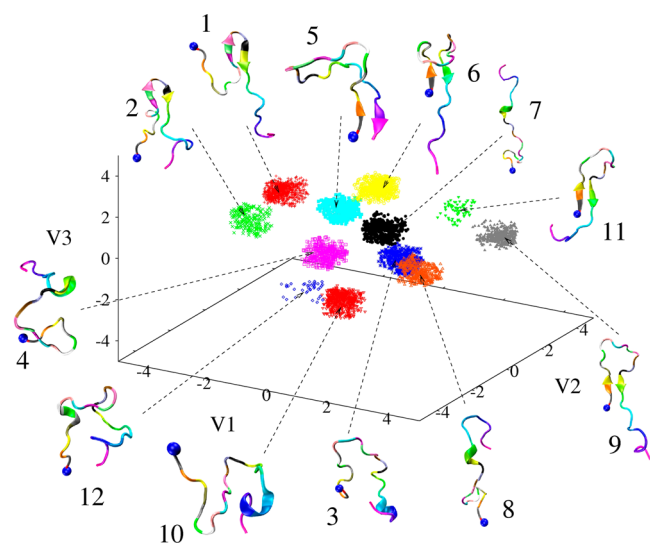


**Figure 5.** 12 clusters of the A2 V peptide on the subspace spanned by the first three principal components V1, V2, and V3. For clarity, only 200 data points around each cluster center are displayed. The representative structure of each cluster is also shown. The ball indicates the first residue. Shown are results obtained using the time interval of 50–205 ns at 315 K.

dominant minima of WT, representing 49% of all conformations, have a  $\beta$ -strand content varying from 4 to 18% and a probability of forming  $\beta$ -hairpins varying from 2 to 6%. Four minima of A2 V have even a probability of forming a three-stranded  $\beta$ -sheet varying from 0.2% (S5) to 1.5% (S6), while only the minimum S13 of WT has a P3s probability of 0.2%. Overall, using the full ensemble of conformations, A $\beta$ 28 A2 V has a much higher population of metastable  $\beta$ -hairpins (13%) than A $\beta$ 28 WT (3%).

The positions of the  $\beta$ -strands in the dominant states of WT and A2 V are shown in Figure 6. In A2 V, the  $\beta$ -hairpin segments with a probability >40% span various positions: 10–13 and 16–20 (S1 and S2), 2–4 and 26–27 (S5), 2–3 and 16–20 (S6), 2–4 and 15–17 (S9), and 2–4 and 16–20 (S11).

In WT, the  $\beta$ -hairpin segments with a probability >40% span the residues 2–3 and 17–19 (S3), 2–5 and 10–15 (S8), 10–12 and 16–19 (S9), 9–11 and 14–20 (S11), 3–4 and 17–19 (S13), and 10–12 and 17–19 (S15). Though the positions of the strands do not match exactly between the peptides, A2 V has a much higher propensity for  $\beta$ -hairpins spanning residues 10–13 and 16–20 than WT. In addition, the  $\beta$ -hairpin spanning 2–4 and 26–27 in WT is not recovered in A2 V and the  $\beta$ -hairpin spanning 2–5 and 10–15 in A2 V is not populated in WT. Looking at the SASA of the amino acid side-chains constituting the  $\beta$ -hairpins (data not shown), the side chains of Phe4, Phe19, and Phe20 are exposed to solvent (SASA > 1.2 nm<sup>2</sup>) in both WT and A2 V peptides, rendering them accessible for intermolecular interactions.

The residue-based  $\alpha$ -helix propensity shows variation from 2% to 14% along both sequences. As shown in Figure 6, the WT peptide can form  $\alpha$ -helices at residues 12–15 in S3 (30% propensity), 15–18 in S4 (20%), 14–19 in S5 (25%), 21–25 in S11 (23%), and 22–25 in S14 (30%). For A2 V peptide, the residues 17–19 display pronounced  $\alpha$ -helix propensity (30%) in the states S4, S5, S10, and S12.

A striking feature in both WT and A2 V peptides is the population of rather fully extended conformations. As shown in Figures 4 and 5 and Table 2, the S6 state in WT, with a population of 7.3%, has an average C $\alpha$  end-to-end distance of 4.5 nm, while the S7 state in A2 V, with a population of 7.8%, has an average C $\alpha$  end-to-end distance of 4.7 nm.

Finally the side-chain contact maps of the two peptides are shown in Figure 7. Unless specified, the probability is calculated using all conformations and all residues in the sequence window. In both systems, the interactions between the first 8 N-terminal residues and the amino acids 22–28 are extremely weak (probability 3%). Both WT and A2 V peptides are characterized by weak side chain interactions between residues 1–6 and 15–20 with a lifetime probability of  $6.6 \pm 0.2\%$ . In WT, the strongest interaction involves Phe4 and Leu17 with a probability of 16%, while in A2 V it is between Val2 and Leu17 with a probability of 18%. The two peptides are also characterized by weak side chain interactions between residues 7–10 and 15–20 with a lifetime probability of  $6.2 \pm 0.2\%$ , in agreement with the high exposure of the side chains to solvent.

#### 4. DISCUSSION

It is of interest to determine, to which extent, our results on the monomer of A $\beta$ 28 WT compare with experiments and previous simulations. Our finding that A $\beta$ 28 WT is essentially coil-turn with 7%  $\alpha$ -helix content is consistent with CD and NMR experiments in aqueous solution reporting a predominant turn-coil character with a  $\alpha$ -helix <10%.<sup>64</sup> Ion-mobility mass-spectrometry (IM-MS) experiments on A $\beta$ 28 WT monomer reported an average distance between the side-chain protons of Arg5 and Lys28 of  $1.75 \pm 0.7$  nm.<sup>65</sup> Using our equilibrium conformations, we find that this interproton distance is  $1.75 \pm 0.9$  nm for WT and  $1.87 \pm 0.9$  nm for A2 V. Diffusion NMR experiments reported a hydrodynamic radius,  $R_h$ , of 1.5 nm for A $\beta$ 28 WT monomer.<sup>66</sup> Given that the characteristic  $R_g/R_h$  value for a globular protein is  $\sim 0.775$ , we can estimate that  $R_g$  should be on the order of 1.1 nm. Using our equilibrium ensemble, we find that  $R_g$  is  $1.03 \pm 0.13$  nm for both peptides. Taken together our simulation reproduces very well the available experimental data on A $\beta$ 28 WT.

Two atomistic REMD simulations with a generalized Born (GB) solvent model have studied the A $\beta$ 28 WT monomer.

Table 2. Characterization of the WT and A2 V Clusters at 315 K<sup>a</sup>

system	cluster	<i>P</i>	$\beta$	helix	turn	coil	<i>P</i> <sub>HB</sub>	<i>P</i> <sub>2s</sub>	<i>d</i> <sub>ee</sub>	RMSD
A2 V	1	12.24	24	4	40.10	31.50	33.52	15.79	3.26	0.00
	2	11.56	17	5	44.32	33.69	27.76	14.95	0.93	0.75
	3	9.94	4	10	50.70	35.77	13.17	9.45	0.89	0.93
	4	9.04	4	11	53.14	31.36	7.86	6.82	1.81	0.95
	5	8.69	16	6	39.90	37.77	24.69	17.53	0.48	1.07
	6	8.10	12	3	43.90	40.94	38.26	23.91	2.01	0.88
	7	7.79	2	9	50.61	38.00	6.05	5.58	4.68	1.12
	8	7.50	9	9	47.42	34.14	6.18	4.97	2.48	0.94
	9	6.99	12	4	45.50	39.18	11.89	11.41	2.23	1.01
	10	6.16	8	11	50.55	30.76	7.48	5.99	2.25	0.89
	11	6.05	16	5	42.67	36.31	47.40	30.09	1.01	1.00
	12	5.95	7	8	48.71	35.45	5.75	5.34	0.90	1.01
WT	1	9.18	8	6	52.10	33.59	6.31	4.52	1.24	0.00
	2	8.94	4	8	53.07	34.43	4.50	3.12	2.73	0.89
	3	8.00	18	8	42.02	32.59	7.15	5.95	0.57	0.91
	4	7.99	4	10	56.96	28.81	3.38	2.92	1.28	0.70
	5	7.98	6	12	46.54	35.60	3.17	2.75	0.79	0.72
	6	7.34	3	9	49.49	38.41	1.97	1.84	4.50	1.33
	7	7.29	3	6	53.97	36.71	1.79	1.59	2.50	0.78
	8	7.11	15	3	41.85	40.48	0.15	0.15	0.15	1.05
	9	6.98	15	5	46.48	33.25	14.88	8.82	1.74	0.67
	10	6.65	10	8	48.22	34.13	1.16	0.97	0.47	0.81
	11	5.56	24	8	39.92	28.65	8.86	6.63	1.01	0.74
	12	5.09	15	3	44.95	36.78	12.74	7.35	2.81	0.82
	13	4.77	16	6	47.13	31.26	7.85	5.33	1.59	0.98
	14	3.62	6	9	50.44	34.91	4.39	2.96	1.72	0.90
	15	3.50	20	2	43.65	33.28	18.56	10.57	1.41	0.84

<sup>a</sup>Representative structures of each cluster are shown on Figures 4 and 5. For each cluster, we show its population (*P* in %), the average value of secondary structure content (in %) and the population of the number of H-bonds between two consecutive  $\beta$ -strands (*P*<sub>HB</sub>, in %). We also show the population of two-stranded  $\beta$ -sheets or  $\beta$ -hairpins (*P*<sub>2s</sub>, in %), the *C* $\alpha$  end-to-end distance (*d*<sub>ee</sub>, in nm), and the *C* $\alpha$  RMSD (in nm) with respect to the first cluster.

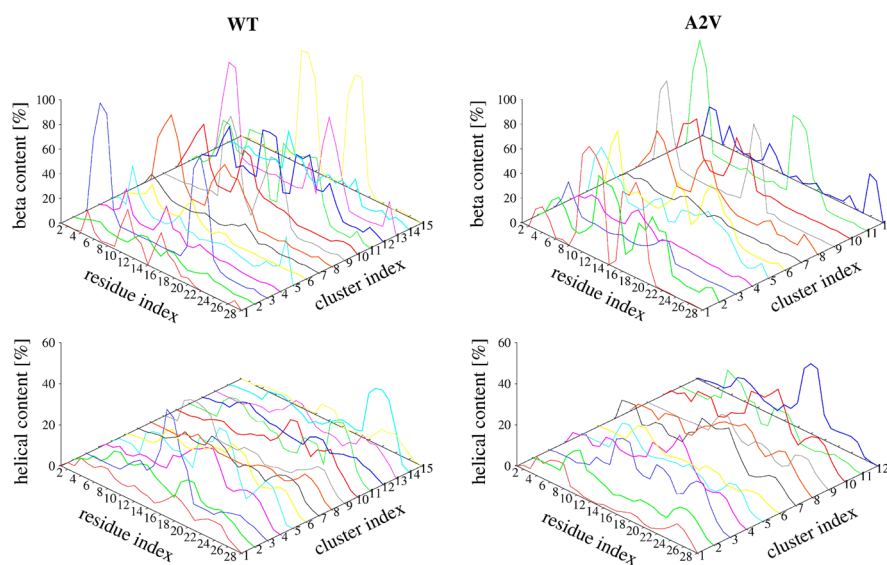


**Figure 6.**  $\beta$ -strand (upper panels) and helical (lower panels) propensities (in %) of each amino acid belonging to the 15 clusters of WT and 12 clusters of A2 V shown in Figures 4 and 5, respectively.

Using a REMD simulation of 50 ns per replica with the CHARMM22 force field with the dihedral cross-term, A $\beta$ 28 WT is mainly unfolded at pH 6 with an averaged  $\alpha$ -helix content of 10%, and three regions, at residues 2–5, 10–13, and 18–22 displaying pronounced helix propensity (10–20% of the time).<sup>67</sup> While their predicted  $\alpha$ -helix content is similar to our

value, our  $\alpha$ -helix content is distributed over residues 2–27, indicating the absence of clear distinct nascent helices. Rather, we find that the two PCA-derived dominant A $\beta$ 28 WT states, each with a probability of 9%, have an average coil–turn of 88%,  $\beta$ -strand of 6% and  $\alpha$ -helix of 7%. Using a REMD with the amber99SB, A $\beta$ 28 WT has an averaged  $\alpha$ -helix of 17% and the



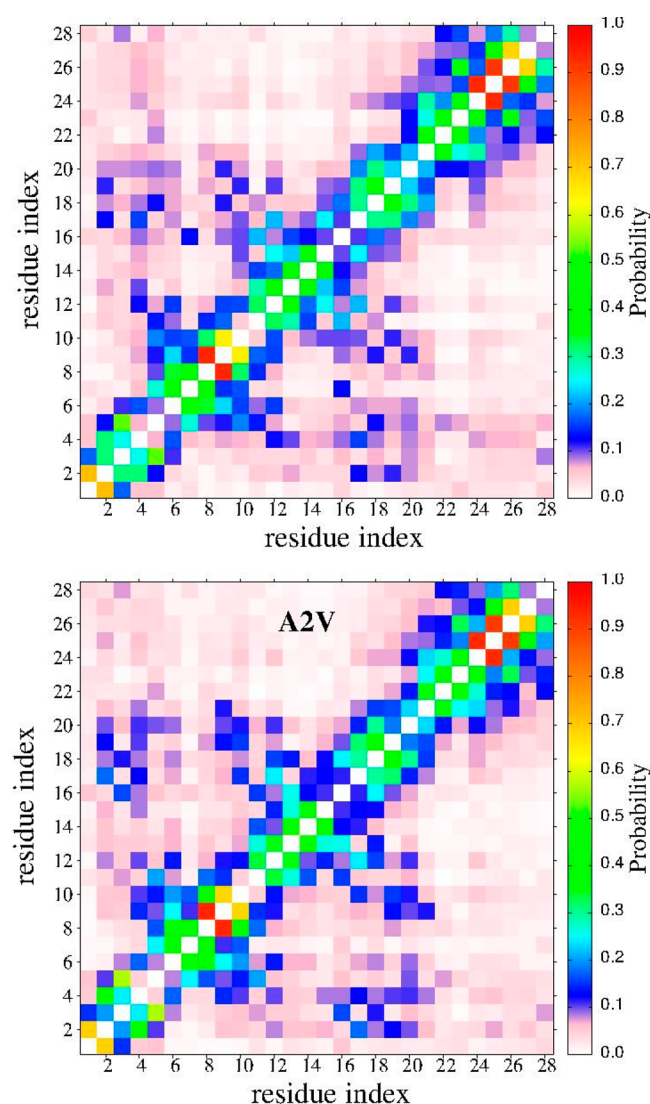


**Figure 7.** Side-chain–side-chain contact maps of the WT (upper) and A2 V (lower) peptides at 315 K using the time interval of 50–205 ns.

Arg5–Gln15 and Lys16–Asp23 regions adopt  $\alpha$ -helix with probabilities of 8–22% and 20–43%.<sup>68</sup> High  $\beta$ -strand formation is determined for the four Arg5, Val12, His13, and Phe19 residues, differing therefore significantly from our minima.

Two coarse-grained (CG) simulations have also studied the A $\beta$ 28 WT monomer. Using the activation-relaxation technique and the OPEP force field, A $\beta$ 28 WT has 75% of residues in random coil and turn, 20% in  $\beta$ -strand and 5% with PPII helix.<sup>18</sup> In agreement with our study, this simulation, although neglecting thermal fluctuations, reports many low energy states characterized by coil- $\beta$ -hairpin and  $\beta$ -hairpin-coil. Their highest  $\beta$ -strand populations at Glu3–Asp5 and Glu11–His13 differ however from our results, where high  $\beta$ -strand signal is found at positions 2–5, 10–13, and 16–20. Using the UNRES CG model and REMD, A $\beta$ 28 WT monomer has an average  $\alpha$ -helix content of 15%, with the residues 13–21 having a probability of 30–40% to adopt  $\alpha$ -helical conformations and residues 4–7 having a 20% to adopt  $\beta$ -strands.<sup>31</sup> The three UNRES-generated typical conformations, one with a  $\alpha$ -helix between Val12 and Glu23, one with a helix between Glu3 and Asp23, and the last with an antiparallel  $\beta$ -sheet spanning Asp1–Val12

followed by a  $\alpha$ -helix between Gln15 and Glu22, are markedly different from our structural ensemble. It remains to be determined whether the most recent OPEP<sup>69,70</sup> and UNRES<sup>71</sup> force fields with more realistic salt-bridge energetic representations fit better our results.

As expected from the intrinsically disordered nature of A $\beta$ , the global free energy minimum of A $\beta$ 28 A2 V and A $\beta$ 28 WT corresponds to an ensemble of turn-coil structures with little  $\alpha$ -helix and  $\beta$ -strand contents. We find that A $\beta$ 28 WT has a high turn probability at residues 6–9, 13–15, and 23–26 (probability 50–60%), consistent with Brooks' results (turn at 23–26),<sup>67</sup> the solution NMR data of the monomer of A $\beta$ 40 WT<sup>72</sup> (turns at 7–11 and 23–27) and recent atomistic REMD simulations of the A $\beta$ 40 WT monomer (turns at 6–9, 14–16, and 24–28).<sup>73</sup> Upon A2 V mutation, there is basically no difference in the turn propensity of the peptide. If the helical content averaged over all residues and conformations is  $7 \pm 1.3\%$  in both WT and A2 V, Figure 6 shows that A2 V shifts the location of transient  $\alpha$ -helix toward the center (namely residues 17–19), while WT can form very transient helices at multiple positions, residues 12–15, 15–18, 14–19, 21–25, or 22–25. Whether this change is significant for A $\beta$  nucleation remains to be determined, even if the transition from  $\alpha$ -helix to  $\beta$ -strand has been proposed to be an important step in the early steps of fibrillogenesis.<sup>13</sup>

The first striking difference between the two species is that the free energy landscape of A $\beta$ 28 A2 V monomer is inverted with respect to the A $\beta$ 28 WT monomer, in that the dominant A2 V states have a high propensity to form  $\beta$ -hairpins while these  $\beta$ -hairpins have a much lower population in the WT states. While the A $\beta$ 28 fibrils form in register parallel  $\beta$ -sheets without any U-shaped conformations, there is strong theoretical evidence on several amyloid peptides that  $\beta$ -hairpins formed in the monomer provide a perfect seed for further growth of the aggregates and reduced lag phases for fibril formation. This is supported by computer simulations on the A $\beta$ 25–35 and A $\beta$ 29–42 peptides,<sup>74,75</sup> the prion protein fragment PrP106–122,<sup>76</sup> the  $\beta$ 2-microglobulin(83–99) peptide,<sup>77</sup> and the human islet amyloid polypeptide hIAPP1–37.<sup>78,79</sup> For instance, atomistic simulations on A $\beta$ 25–35 peptides showed that, although the monomer preferentially adopts a  $\beta$ -hairpin conformation, a clear transition from compact  $\beta$ -hairpin conformations to extended  $\beta$ -strand structures occurs between dimers and trimer.<sup>74</sup>

The second striking result is that the pathological A2 V mutation, enhancing the aggregation propensity of A $\beta$ 40, has a considerable impact on the conformational landscape of the protein, thereby affecting its intrinsic disorder. Here, we find that upon A2 V mutation, the intrinsic disorder of A $\beta$ 28 monomer is reduced by a factor of 2 and the equilibrium ensemble is completely changed. This result is in perfect agreement with the recent De Simone–Dobson–Frenkel model where a generic link was found between intrinsic disorder and protein self-assembly and aggregation.<sup>80</sup> Using multiscale simulations, De Simone et al. found that the presence of highly flexible regions may act to suppress very significantly the tendency of proteins to aggregate. Our result goes however one step ahead by linking change in intrinsic disorder with pathological mutation and indicating that the A2 V mutation influences not only the N-terminus but the whole A $\beta$ 28 peptide.

## 5. CONCLUSIONS

Laser light scattering measurements over short periods (first 24 h after sample preparation) showed that the aggregation kinetics is four times faster for A $\beta$ 40 A2 V than for A $\beta$ 40 WT.<sup>35</sup> Though A $\beta$ 28 forms fibrils at a lower rate than A $\beta$ 40 fibrils,<sup>81</sup> we believe that A $\beta$ 28 is a good model to understand the impact of A2 V on A $\beta$ 40 for the following reasons. All charged or polar side-chains of A $\beta$ 40 are located in the first 28 residues of the N-terminal and this may explain why small compounds bind similarly to A $\beta$ 40 and A $\beta$ 28 peptides.<sup>41</sup> Mice, differing from human A $\beta$ 42 sequence by three mutations R5G, Y10F and H13R, never develop AD.<sup>82</sup> Last but not least, our simulations on both WT and A2 V show that there are very weak and transient interactions between the side-chains of the N-terminus and the side-chains of the CHC and FL regions. This result is consistent with two recent atomistic simulations of A $\beta$ 40 monomer<sup>42,83</sup> and is also supported by two recent experimental studies. A hydrogen–deuterium exchange coupled to mass spectrometry study showed that the region (residues 1–19) is the last to aggregate during A $\beta$ 42 oligomerization,<sup>84</sup> and the solution structure of A $\beta$ 40 in complex with Z(A $\beta$ 3), a binding protein of nanomolar affinity, showed a  $\beta$ -hairpin structure spanning 16–36 with the residues 1–15 disordered.<sup>85</sup>

In summary, we have shown that the equilibrium ensemble of A $\beta$ 28 WT monomer fits nicely with CD, IM-MS and diffusion NMR data, validating therefore our REMD simulation using the CHARMM22\* force field and a standard experimental phosphate buffer. Interestingly for both peptides, our atomistic simulations reveal for the first time to the best of our knowledge the existence of extended metastable conformations with end-to-end-distances of 4.5–4.7 nm. It is clear that these states represent ideal seeds for A $\beta$ 28 polymerization, and might potentially seed aggregation of A $\beta$ 40.

While the CHARMM22\* force field allows folding diverse monomeric proteins of 12–70 amino acids into their NMR structures,<sup>47</sup> providing therefore one cluster with a high Boltzmann probability, its application to A $\beta$ 28 WT monomer leads to two thousands of clusters. Upon A2 V mutation, the population of  $\beta$ -hairpins is increased by a factor of 4, and this is clearly one factor contributing to the higher aggregation propensity of A $\beta$ 40 A2 V. A second important consequence of A2 V is that the intrinsic disorder of A $\beta$ 28 monomer is reduced by a factor of 2, and this can also explain the higher aggregation propensity of A $\beta$ 40 A2 V.

Even more strikingly the equilibrium ensemble of A $\beta$ 28 A2 V is totally different from that of A $\beta$ 28 WT. In the context of protein–protein recognition, the “lock-and-key” mechanism postulates that each partner essentially binds in its lowest energy state.<sup>86</sup> The “conformational selection” model posits that many protein conformations including the bound state pre-exist, and the binding interaction leads to a Boltzmann population shift, redistributing the conformational states.<sup>87</sup> In contrast, the “induced-fit” model postulates that the bound protein conformation forms only after interaction with a binding partner.<sup>86,87</sup> Clearly, the total difference in the conformational ensembles of WT and A2 V exclude the first two recognition models, and this might already explain why the mixture of the WT and A2 V peptides and the A2 V mutation protect against AD when one copy of the gene is present. It remains to be determined, however, whether the induced-fit model applies when the WT and A2 V peptides are mixed. To

this end, we are currently performing REMD simulations of the dimer of A $\beta$ 40 WT and the dimer of A $\beta$ 40 WT-A2 V.

## AUTHOR INFORMATION

### Corresponding Author

\*E-mail: philippe.derreumaux@ibpc.fr. Tel: 33 1 58 41 51 72.

### Notes

The authors declare no competing financial interest.

## ACKNOWLEDGMENTS

This work was supported by grants from the “GRAL” ANR SIMI 12-BS07-0017-01 and Pierre Gilles de Gennes Foundation. We also acknowledge equipment support from “DYNAMO” ANR-11-LABX-0011.

## REFERENCES

- (1) Selkoe, D. J. Folding Proteins in Fatal Ways. *Nature* **2003**, *426*, 900–904.
- (2) Aisen, P. S.; Vellas, B.; Hampel, H. Moving Towards Early Clinical Trials for Amyloid Targeted Therapy in Alzheimer's Disease. *Nat. Rev. Drug Discovery* **2013**, *12*, 324–325.
- (3) Qiang, W.; Kelley, K.; Tycko, R. Polymorph-Specific Kinetics and Thermodynamics of  $\beta$ -Amyloid Fibril Growth. *J. Am. Chem. Soc.* **2013**, *135*, 6860–6871.
- (4) Tycko, R.; Wickner, R. B. Molecular Structures of Amyloid and Prion Fibrils: Consensus Versus Controversy. *Acc. Chem. Res.* **2013**, *46*, 1487–1496.
- (5) Kirkitadze, M. D.; Condrón, M. M.; Teplow, D. B. Identification and Characterization of Key Kinetic Intermediates in Amyloid  $\beta$ -Protein Fibrillogenesis. *J. Mol. Biol.* **2001**, *312*, 1103–1119.
- (6) Kaden, D.; Harmeier, A.; Weise, C.; Munter, L. M.; Althoff, V.; Rost, B. R.; Hildebrand, P. W.; Schmitz, D.; Schaefer, M.; Lurz, R.; et al. Novel APP/A $\beta$  Mutation K16N Produces Highly Toxic Heteromeric A $\beta$  Oligomers. *EMBO Mol. Med.* **2012**, *4*, 647–659.
- (7) Lu, J.-X.; Qiang, W.; Yau, W.-M.; Schwieters, C. D.; Meredith, S. C.; Tycko, R. Molecular Structure of  $\beta$ -Amyloid Fibrils in Alzheimer's Disease Brain Tissue. *Cell* **2013**, *154*, 1257–1268.
- (8) Masters, C. L.; Selkoe, D. J. Biochemistry of Amyloid  $\beta$ -Protein and Amyloid Deposits in Alzheimer Disease. *Cold Spring Harb. Perspect. Med.* **2012**, *2*, a006262.
- (9) Qahwash, I.; Weiland, K. L.; Lu, Y.; Sarver, R. W.; Kletzien, R. F.; Yan, R. Identification of a Mutant Amyloid Peptide that Predominantly Forms Neurotoxic Protofibrillar Aggregates. *J. Biol. Chem.* **2003**, *278*, 23187–23195.
- (10) Dorlet, P.; Gambarelli, S.; Faller, P.; Hureau, C. Pulse EPR Spectroscopy Reveals the Coordination Sphere of Copper(II) Ions in the 1–16 Amyloid- $\beta$  Peptide: A Key Role of the First two N-Terminus Residues. *Angew. Chem., Int. Ed. Engl.* **2009**, *48*, 9273–9276.
- (11) Wakutani, Y.; Watanabe, K.; Adachi, Y.; Wada-Isoe, K.; Urakami, H.; Ninomiya, H.; Saido, T. C.; Hashimoto, T.; Iwatsubo, T.; Nakashima, K. Novel Amyloid Precursor Protein Gene Missense Mutation (D678N) in Probable Familial Alzheimer's Disease. *J. Neurol. Neurosurg. Psychiatry* **2004**, *75*, 1039–1042.
- (12) Janssen, J. C.; Beck, J. A.; Campbell, T. A.; Dickinson, A.; Fox, N. C.; Harvey, R. J.; Houlden, H.; Rossor, M. N.; Collinge, J. Early Onset Familial Alzheimer's Disease: Mutation Frequency in 31 Families. *Neurology* **2003**, *60*, 235–239.
- (13) Ono, K.; Condrón, M. M.; Teplow, D. B. Effects of the English (H6R) and Tottori (D7N) Familial Alzheimer Disease Mutations on Amyloid  $\beta$ -Protein Assembly and Toxicity. *J. Biol. Chem.* **2010**, *285*, 23186–23197.
- (14) Melquiond, A.; Dong, X.; Mousseau, N.; Derreumaux, P. Role of the Region 23–28 in A $\beta$  Fibril Formation: Insights from Simulations of the Monomers and Dimers of Alzheimer Peptides A $\beta$ 40 and A $\beta$ 42. *Curr. Alzheimer Res.* **2008**, *5*, 244–250.
- (15) Urbanc, B.; Betnel, M.; Cruz, L.; Bitan, G.; Teplow, D. B. Elucidation of Amyloid  $\beta$ -Protein Oligomerization Mechanisms:



Discrete Molecular Dynamics Study. *J. Am. Chem. Soc.* **2010**, *132*, 4266–4282.

(16) Côté, S.; Laghaei, R.; Derreumaux, P.; Mousseau, N. Distinct Dimerization for Various Alloforms of the Amyloid- $\beta$  Protein:  $A\beta(1-40)$ ,  $A\beta(1-42)$ , and  $A\beta(1-40)(D23N)$ . *J. Phys. Chem. B* **2012**, *116*, 4043–4055.

(17) Côté, S.; Derreumaux, P.; Mousseau, N. Distinct Morphologies for Amyloid  $\beta$  Monomer:  $A\beta(1-40)$ ,  $A\beta(1-42)$  and  $A\beta(1-40)(D23N)$ . *J. Chem. Theory Comput.* **2011**, *7*, 2584–2592.

(18) Dong, X.; Chen, W.; Mousseau, N.; Derreumaux, P. Energy Landscapes of the Monomer and Dimer of the Alzheimer's Peptide  $A\beta(1-28)$ . *J. Chem. Phys.* **2008**, *128*, 125108.

(19) Santini, S.; Mousseau, N.; Derreumaux, P. Silico Assembly of Alzheimer's  $A\beta(16-22)$  Peptide into  $\beta$ -sheets. *J. Am. Chem. Soc.* **2004**, *126*, 11509–11516.

(20) Santini, S.; Wei, G.; Mousseau, N.; Derreumaux, P. Pathway Complexity of Alzheimer's  $\beta$ -Amyloid  $A\beta(16-22)$ . *Structure* **2004**, *12*, 1245–1255.

(21) Mousseau, N.; Derreumaux, P. Exploring the Early Steps of Amyloid Peptide Aggregation by Computers. *Acc. Chem. Res.* **2005**, *38*, 885–891.

(22) Melquiond, A.; Mousseau, N.; Derreumaux, P. Structure of Soluble Amyloid Oligomers from Computer Simulations. *Proteins* **2006**, *65*, 180–191.

(23) Song, W.; Wei, G.; Mousseau, N.; Derreumaux, P. Self-Assembly of the  $\beta$ 2-Microglobulin NHVTLSSQ Peptide Using a Coarse-Grained Protein Model Reveals  $\beta$ -Barrel Species. *J. Phys. Chem. B* **2008**, *112*, 4410–4418.

(24) Laganowsky, A.; Liu, C.; Sawaya, M. R.; Whitelegge, J. P.; Park, J.; Zhao, M.; Pensalfini, A.; Soriaga, A. B.; Landau, M.; Teng, P. K.; et al. Atomic View of a Toxic Amyloid Small Oligomer. *Science* **2012**, *335*, 1228–1231.

(25) De Simone, A.; Derreumaux, P. Low Molecular Weight Oligomers of Amyloid Peptides Display  $\beta$ -Barrel Conformations: A Replica Exchange Molecular Dynamics Study in Explicit Solvent. *J. Chem. Phys.* **2010**, *132*, 165103.

(26) Chebaro, Y.; Derreumaux, P. Targeting the Early Steps of  $A\beta(16-22)$  Protofibril Disassembly by N-Methylated Inhibitors: A Numerical Study. *Proteins* **2009**, *75*, 442–452.

(27) Lu, Y.; Derreumaux, P.; Guo, Z.; Mousseau, N.; Wei, G. Thermodynamics and Dynamics of Amyloid Peptide Oligomerization are Sequence Dependent. *Proteins* **2009**, *75*, 954–963.

(28) Liu, C.; Sawaya, M. R.; Cheng, P. N.; Zheng, J.; Nowick, J. S.; Eisenberg, D. Characteristics of Amyloid-Related Oligomers Revealed by Crystal Structures of Macrocyclic  $\beta$ -Sheet Mimics. *J. Am. Chem. Soc.* **2011**, *133*, 6736–6744.

(29) Ma, B.; Nussinov, R. Polymorphic Triple  $\beta$ -Sheet Structures Contribute to Amide Hydrogen/Deuterium (H/D) Exchange Protection in the Alzheimer Amyloid  $\beta$ 42 Peptide. *J. Biol. Chem.* **2011**, *286*, 34244–34253.

(30) Lopez del Amo, J. M.; Schmidt, M.; Fink, U.; Dasari, M.; Fändrich, M.; Reif, B. An Asymmetric Dimer as the Basic Subunit in Alzheimer's Disease Amyloid  $\beta$  Fibrils. *Angew. Chem., Int. Ed. Engl.* **2012**, *51*, 6136–6139.

(31) Lv, Z.; Roychaudhuri, R.; Condrón, M. M.; Teplow, D. B.; Lyubchenko, Y. L. Mechanism of Amyloid  $\beta$ -Protein Dimerization Determined Using Single-Molecule AFM Force Spectroscopy. *Sci. Rep.* **2013**, *3*, 2880.

(32) Rojas, A. V.; Liwo, A.; Scheraga, H. A. A Study of the  $\alpha$ -Helical Intermediate Preceding the Aggregation of the Amino-Terminal Fragment of the  $\beta$  Amyloid Peptide ( $A\beta(1-28)$ ). *J. Phys. Chem. B* **2011**, *115*, 12978–12983.

(33) Zhang, T.; Zhang, J.; Derreumaux, P.; Mu, Y. Molecular Mechanism of the Inhibition of EGCG on the Alzheimer  $A\beta(1-42)$  Dimer. *J. Phys. Chem. B* **2013**, *117*, 3993–4002.

(34) Zhang, T.; Zhang, J.; Mu, Y. Derreumaux, P. Atomic and Dynamic Insights into the Beneficial Effect of the 1,4-Naphthoquinone-2-yl-L-tryptophan Inhibitor on Alzheimer's  $A\beta(1-42)$  dimer in Terms of

Aggregation and Toxicity. *ACS Chem. Neurosci.* **2013** DOI: 10.1021/cn400197x

(35) Di Fede, G.; Catania, M.; Morbin, M.; Rossi, G.; Suardi, S.; Mazzoleni, G.; Merlin, M.; Giovagnoli, A. R.; Prioni, S.; Erbetta, A.; et al. A Recessive Mutation in the APP Gene with Dominant-Negative Effect on Amyloidogenesis. *Science* **2009**, *323*, 1473–1477.

(36) Jonsson, T.; Atwal, J. K.; Steinberg, S.; Snaedal, J.; Jonsson, P. V.; Björnsson, S.; Stefansson, H.; Sulem, P.; Gudbjartsson, D.; Maloney, J.; et al. A Mutation in APP Protects Against Alzheimer's Disease and Age-Related Cognitive Decline. *Nature* **2012**, *488*, 96–99.

(37) Pellarin, R.; Schuetz, P.; Guarnera, E.; Caffisch, A. Amyloid Fibril Polymorphism is Under Kinetic Control. *J. Am. Chem. Soc.* **2010**, *132*, 14960–14970.

(38) Li, M.; Co, N.; Reddy, G.; Hu, C.; Straub, E.; Thirumalai, D. Factors Governing Fibrillogenesis of Polypeptide Chains Revealed by Lattice Models. *Phys. Rev. Lett.* **2010**, *105*, 218101.

(39) Mikros, E.; Benaki, D.; Humpfer, E.; Spraul, M.; Loukas, S.; Stassinopoulou, C. I.; Pelecanou, M. High-Resolution NMR Spectroscopy of the  $\beta$ -Amyloid (1–28) Fibril Typical for Alzheimer's Disease. *Angew. Chem., Int. Ed. Engl.* **2001**, *40*, 3603–3605.

(40) Moore, B. D.; Chakrabarty, P.; Levites, Y.; Kukar, T. L.; Baine, A. M.; Moroni, T.; Ladd, T. B.; Das, P.; Dickson, D. W.; Golde, T. E. Overlapping profiles of  $A\beta$  peptides in the Alzheimer's disease and pathological aging brains. *Alzheimers Res. Ther.* **2012**, *4*, 18.

(41) Martineau, E.; de Guzman, J. M.; Rodionova, L.; Kong, X.; Mayer, P. M.; Aman, A. M. Investigation of the Noncovalent Interactions between Anti-Amyloid Agents and Amyloid  $\beta$  Peptides by ESI-MS. *J. Am. Soc. Mass. Spectrom.* **2010**, *21*, 1506–1514.

(42) Lin, Y. S.; Pande, V. S. Effects of Familial Mutations on the Monomer Structure of  $A\beta$ 42. *Biophys. J.* **2012**, *103*, L47–49.

(43) Huet, A.; Derreumaux, P. Impact of the Mutation A21G (Flemish Variant) on Alzheimer's  $\beta$ -Amyloid Dimers by Molecular Dynamics Simulations. *Biophys. J.* **2006**, *91*, 3829–3840.

(44) Shea, J. E.; Urbanc, B. Insights into  $A\beta$  Aggregation: A Molecular Dynamics Perspective. *Curr. Top. Med. Chem.* **2012**, *12*, 2596–2610.

(45) Viet, M. H.; Nguyen, P. H.; Ngo, S. T.; Li, M. S.; Derreumaux, P. Effect of the Tottori Familial Disease Mutation (D7N) on the Monomers and Dimers of  $A\beta$ 40 and  $A\beta$ 42. *ACS Chem. Neurosci.* **2013**, *4*, 1446–1457.

(46) Coles, M.; Bicknell, W.; Watson, A. A.; Fairlie, D. P.; Craik, D. J. Solution Structure of Amyloid  $\beta$ -Peptide(1–40) in a Water-Micelle Environment. Is the Membrane-Spanning Domain Where We Think It Is? *Biochemistry* **1998**, *37*, 11064–11077.

(47) Nguyen, P. H.; Li, M. S.; Derreumaux, P. Effects of All-Atom Force Fields on Amyloid Oligomerization: Replica Exchange Molecular Dynamics Simulations of the  $A\beta(16-22)$  Dimer and Trimer. *Phys. Chem. Chem. Phys.* **2011**, *13*, 9778–9788.

(48) Lindorff-Larsen, K.; Piana, S.; Dror, R. O.; Shaw, D. E. How Fast-Folding Proteins Fold. *Science* **2011**, *334*, 517–520.

(49) Derreumaux, P.; Dauchez, M.; Vergoten, G. The Structures and Vibrational Frequencies of a Series of Alkanes Using the SPASIBA Force Field. *J. Mol. Struct.* **1993**, *295*, 203–221.

(50) Derreumaux, P.; Vergoten, G.; Lagant, P. A Vibrational Molecular Force Field of Model Compounds with Biological Interest. I. Harmonic Dynamics of Crystalline Urea at 123 K. *J. Comput. Chem.* **1990**, *11*, S60–S68.

(51) Derreumaux, P.; Vergoten, G. A New Spectroscopic Molecular Mechanics Force Field. Parameters for Proteins. *J. Chem. Phys.* **1995**, *102*, 8586–8605.

(52) Berendsen, H. J. C.; van der Spoel, D.; van Drunen, R. GROMACS: A Message-Passing Parallel Molecular Dynamics Implementation. *Comput. Phys. Commun.* **1995**, *91*, 43–56.

(53) Ryckaert, J.-P.; Ciccotti, G.; Berendsen, H. J. C. Numerical Integration of the Cartesian Equations of Motion of a System with Constraints: Molecular Dynamics of n-Alkanes. *J. Comput. Phys.* **1977**, *23*, 327–341.

(54) Bussi, G.; Donadio, D.; Parrinello, M. Canonical Sampling Through Velocity Rescaling. *J. Chem. Phys.* **2007**, *126*, 014101.

- (55) The PyMOL Molecular Graphics System, Version 1.5.0.4 Schrödinger, LLC.
- (56) Patriksson, A.; van der Spoel, D. A Temperature Predictor for Parallel Tempering Simulations. *Phys. Chem. Chem. Phys.* **2008**, *10*, 2073–2077.
- (57) Frishman, D.; Argos, P. Knowledge-Based Protein Secondary Structure Assignment. *Proteins* **1995**, *23*, 566–579.
- (58) Amadei, A.; Linssen, A. B. M.; Berendsen, H. J. C. Essential Dynamics of Proteins. *Proteins* **1993**, *17*, 412–425.
- (59) Hartigan, J. A.; Wong, M. A. A k-Means Clustering Algorithm. *Appl. Statist.* **1979**, *28*, 100–108.
- (60) R Development Core Team. R: A language and environment for statistical computing; R Foundation for Statistical Computing: Vienna, Austria, 2008; <http://www.R-project.org>.
- (61) Altis, A.; Otten, M.; Nguyen, P. H.; Hegger, R.; Stock, G. Construction of the Free Energy Landscape of Biomolecules Via Dihedral Angle Principal Component Analysis. *J. Chem. Phys.* **2008**, *128*, 245102.
- (62) Charrad, M.; Ghazzali, N.; Boiteau, V.; Niknafs, A. An examination of indices for determining the number of clusters: NbClust Package, version 1.4, 2013; <http://cran.r-project.org/web/packages/NbClust>.
- (63) Izuo, N.; Kume, T.; Sato, M.; Murakami, K.; Irie, K.; Izumi, Y.; Akaike, A. Toxicity in Rat Primary Neurons Through the Cellular Oxidative Stress Induced by the Turn Formation at Positions 22 and 23 of A $\beta$ 42. *ACS Chem. Neurosci.* **2012**, *3*, 674–681.
- (64) Barrow, C. J.; Yasuda, A.; Kenny, P. T. M.; Zagorski, M. G. Solution Conformations and Aggregational Properties of Synthetic Amyloid  $\beta$ -Peptides of Alzheimer's Disease. Analysis of Circular Dichroism Spectra. *J. Mol. Biol.* **1992**, *225*, 1075–1093.
- (65) Li, A.; Fenselau, C. Contact Regions in the Dimer of Alzheimer  $\beta$ -Amyloid Domain [1–28] Studied by Mass Spectrometry. *Eur. J. Mass Spectrom.* **2004**, *10*, 309–316.
- (66) Talmard, C.; Guilloreau, L.; Coppel, Y.; Mazarguil, H.; Faller, P. Amyloid- $\beta$  Peptide Forms Monomeric Complexes with Cu<sup>II</sup> and Zn<sup>II</sup> Prior to Aggregation. *ChemBioChem* **2007**, *8*, 163–165.
- (67) Khandogin, J.; Brooks, C. L., 3rd Linking Folding with Aggregation in Alzheimer's  $\beta$ -Amyloid Peptides. *Proc. Natl. Acad. Sci. U.S.A.* **2007**, *104*, 16880–16885.
- (68) Wise-Scira, O.; Xu, L.; Kitahara, T.; Perry, G.; Coskuner, O. Amyloid- $\beta$  peptide structure in aqueous solution varies with fragment size. *J. Chem. Phys.* **2011**, *135*, 205101.
- (69) Chebaro, Y.; Pasquali, S.; Derreumaux, P. The Coarse-Grained OPEP Force Field for Non-Amyloid and Amyloid Proteins. *J. Phys. Chem. B* **2012**, *116*, 8741–8752.
- (70) Sterpone, F.; Nguyen, P. H.; Kalimeri, M.; Derreumaux, P. Importance of the Ion-Pair Interactions in the OPEP Coarse-Grained Force Field: Parametrization and Validation. *J. Chem. Theory Comput.* **2013**, *9*, 4574–4584.
- (71) Makowski, M.; Liwo, A.; Scheraga, H. A. Simple Physics-Based Analytical Formulas for the Potentials of Mean Force of the Interaction of Amino-Acid Side Chains in Water. VI. Oppositely Charged Side Chains. *J. Phys. Chem. B* **2011**, *115*, 6130–6137.
- (72) Laurents, D. V.; Gorman, P. M.; Guo, M.; Rico, M.; Chakrabarty, A.; Bruix, M. Alzheimer's A $\beta$ 40 Studied by NMR at Low pH Reveals that DSS Binds and Promotes  $\beta$ -Ball Oligomerization. *J. Biol. Chem.* **2005**, *280*, 3675–3685.
- (73) Rosenman, D. J.; Connors, C. R.; Chen, W.; Wang, C.; García, A. E. A $\beta$  Monomers Transiently Sample Oligomer and Fibril-Like Configurations: Ensemble Characterization Using a Combined MD/NMR Approach. *J. Mol. Biol.* **2013**, *425*, 3338–3359.
- (74) Larini, L.; Shea, J. E. Role of  $\beta$ -Hairpin Formation in Aggregation: The Self-Assembly of the Amyloid- $\beta$ (25–35) Peptide. *Biophys. J.* **2012**, *103*, 576–586.
- (75) Lu, Y.; Wei, G.; Derreumaux, P. Effects of G33A and G33I mutations on the structures of monomer and dimer of the amyloid- $\beta$  fragment 29–42 by replica exchange molecular dynamics simulations. *J. Phys. Chem. B* **2011**, *115*, 1282–8.
- (76) Grabenauer, M.; Wu, C.; Soto, P.; Shea, J. E.; Bowers, M. T. Oligomers of the Prion Protein Fragment 106–126 Are Likely Assembled from  $\beta$ -Hairpins in Solution, and Methionine Oxidation Inhibits Assembly without Altering the Peptide's Monomeric Conformation. *J. Am. Chem. Soc.* **2010**, *132*, 532–539.
- (77) Liang, C.; Derreumaux, P.; Wei, G. Structure and aggregation mechanism of  $\beta$ 2-microglobulin (83–99) peptides studied by molecular dynamics simulations. *Biophys. J.* **2007**, *93*, 3353–62.
- (78) Qiao, Q.; Bowman, G. R.; Huang, X. Dynamics of an Intrinsically Disordered Protein Reveal Metastable Conformations That Potentially Seed Aggregation. *J. Am. Chem. Soc.* **2013**, *135*, 16092–16101.
- (79) Wu, C.; Shea, J. E. Structural Similarities and Differences between Amyloidogenic and Non-Amyloidogenic Islet Amyloid Polypeptide (IAPP) Sequences and Implications for the Dual Physiological and Pathological Activities of These Peptides. *PLoS Comput. Biol.* **2013**, *9*, e1003211.
- (80) De Simone, A.; Kitchen, C.; Kwan, A. H.; Sunde, M.; Dobson, C. M.; Frenkel, D. Intrinsic disorder modulates protein self-assembly and aggregation. *Proc. Natl. Acad. Sci. U.S.A.* **2012**, *109*, 6951–6.
- (81) De Felice, F. G.; Houzel, J. C.; Garcia-Abreu, J.; Louzada, P. R., Jr.; Afonso, R. C.; Meirelles, M. N.; Lent, R.; Neto, V. M.; Ferreira, S. T. Inhibition of Alzheimer's disease beta-amyloid aggregation, neurotoxicity, and in vivo deposition by nitrophenols: implications for Alzheimer's therapy. *FASEB J.* **2001**, *15*, 1297–9.
- (82) Lv, X.; Li, W.; Luo, Y.; Wang, D.; Zhu, C.; Huang, Z. X.; Tan, X. Exploring the Differences between Mouse mA $\beta$ (1–42) and Human hA $\beta$ (1–42) for Alzheimer's Disease Related Properties and Neuronal Cytotoxicity. *Chem. Commun.* **2013**, *49*, 5865–5867.
- (83) Ball, K. A.; Phillips, A. H.; Wemmer, D. E.; Head-Gordon, T. Differences in  $\beta$ -strand populations of monomeric A $\beta$ 40 and A $\beta$ 42. *Biophys. J.* **2013**, *104*, 2714–24.
- (84) Zhang, Y.; Rempel, D. L.; Zhang, J.; Sharma, A. K.; Mirica, L. M.; Gross, M. L. Pulsed hydrogen-deuterium exchange mass spectrometry probes conformational changes in amyloid  $\beta$  (A $\beta$ ) peptide aggregation. *Proc. Natl. Acad. Sci. U.S.A.* **2013**, *110*, 14604–14609.
- (85) Hoyer, W.; Grönwall, C.; Jonsson, A.; Ståhl, S.; Hård, T. Stabilization of a  $\beta$ -Hairpin in Monomeric Alzheimer's Amyloid- $\beta$  Peptide Inhibits Amyloid Formation. *Proc. Natl. Acad. Sci. U.S.A.* **2008**, *105*, 5099–5104.
- (86) Tuffery, P.; Derreumaux, P. Flexibility and binding affinity in protein-ligand, protein-protein and multi-component protein interactions: limitations of current computational approaches. *J. R. Soc. Interface.* **2012**, *9*, 20–33.
- (87) Boehr, D. D.; Nussinov, R.; Wright, P. E. The role of dynamic conformational ensembles in biomolecular recognition. *Nat. Chem. Biol.* **2009**, *5*, 789–96.